How to cite: *Angew. Chem. Int. Ed.* **2025**, e22967
doi.org/10.1002/anie.202522967

Enzyme Immobilization in MOFs | **Very Important Paper**

Monitoring Enzyme Clustering in a Highly Crystalline Metal–Organic Framework by Small-Angle Neutron Scattering

Xiaoliang Wang, Lilin He, Shuo Qian, Shengyi Su, Omar K. Farha,* and Shengqian Ma**

Abstract: The molecular-level investigation of enzyme behavior in confined, cell-free environments is essential to understanding intrinsic properties and optimizing systems for desired functions. Metal–organic frameworks (MOFs) provide unique structural features that enable the immobilization of bulky biomolecules and allow direct probing of enzymatic behavior under confinement. Here, small-angle neutron scattering (SANS) was employed to probe porosity changes in a highly crystalline Tb-mesoMOF and to reveal the spatial arrangement of encapsulated enzymes across long-range length scales. Structural characteristics such as framework void space were resolved by SANS, while contrast-matching experiments using D_2O/H_2O mixtures suppressed background scattering from the MOF and isolated the enzyme contribution. Compared to unloaded Tb-mesoMOF, cytochrome c (Cyt. c)-loaded Tb-mesoMOF exhibited the emergence of a broad scattering feature at low q (~0.005 $Å^{-1}$), indicative of enzyme clustering within the framework, accompanied by enhanced loading rate and capacity. Additional structural analyses using complementary techniques further corroborated these findings.

Introduction

Confinement of enzymes has a substantial influence on their functions and stability, and dramatically enhances their feasibility in industrial processes due to low structural dynamics, reduced product/substrate inhibition, and minimal leaching behaviors.[1–6] The immobilization of enzymes in metal-organic frameworks (MOFs) has gained burgeoning attention in fundamental and industrial research, due to the remarkable structural properties of MOFs, like high crystallinity, the large yet adjustable pore structures.[7–12] Although significant progress has been made in overcoming the intrinsic limitations of enzymes in stability and recyclability, a fundamental gap remains in understanding how confinement environments influence enzyme arrangement and in developing strategies to improve their accommodation efficiency.

Recent studies have repeatedly highlighted that enzyme structural alterations, spatial arrangement, and host-guest interactions play critical roles in regulating enzymatic performance under confined environments.[13–16] Interestingly, previous studies have proposed that oversized biomolecules may adjust themselves during translocation into MOFs, as their inherent conformational flexibility allows passage through pore apertures.[17–19] However, growing evidence suggests that defects in MOFs also play a critical role in the enzyme immobilization in addition to intrinsic nanoscale porosity.[20–24] MOF defects can arise due to several factors, including synthetic conditions, activation process, and external stimuli.[25–29] Depending on the application, these defects can be either beneficial or detrimental. For enzyme immobilization, certain defects can enhance enzyme loading efficiency and activity by providing additional transport pathways and binding sites, thereby enabling the rapid accommodation of larger and/or more complex biofunctionalities. Despite this, only a few studies have clearly observed the formation of enzyme aggregation or clustering within MOF,[30,31] and explored the impact of pore microenvironment on enzyme loading efficiency.[20,22] For example, our previous work of site-directed spin labelling (SDSL) EPR has exhibited high feasibility in clarifying the structure and dynamics of conformationally constrained model lysozyme (T4L) in channel-type MOF/COF/porous silica (PCN-128, COF-ETTA-TPDA and MCM-41).[19] It unveiled the specific interplays among enzymes and enzyme-MOF, resulting in preferred enzyme orientation and close packing density under distinct microenvironments (*e.g.*, charge state and hydrophobicity). However, the longstanding challenge in directly observing such behaviors still exists. One reason is the large molecular scale of enzymes, which results in a high degree of structural flexibility and typically causes them to be amorphous and randomly orientated within the pores. Furthermore, the weak and complex enzyme-

[*] Prof. S. Ma
Department of Chemistry, University of North Texas, Denton, Texas 76201, USA
E-mail: Shengqian.Ma@unt.edu

Dr. L. He, Dr. S. Qian
Neutron Scattering Division, Oak Ridge National Laboratory, Oak Ridge, Tennessee 37831, USA
E-mail: hel3@ornl.gov

Dr. X. Wang, S. Su, Prof. O. K. Farha
Department of Chemistry, Northwestern University, Evanston, Illinois 60208, USA
E-mail: o-farha@northwestern.edu

Prof. O. K. Farha
Department of Chemical and Biological Engineering, Northwestern University, Evanston, Illinois 60208, USA

Additional supporting information can be found online in the Supporting Information section

matrix interactions in MOFs are difficult to characterize via traditional techniques. In preceding studies, the technique of small-angle neutron scattering (SANS) was used to study the size and shape of scattering particles in solution,[32,33] and examine the confinement effects on guest behaviors in ordered mesoporous silica materials like MCM-41 and SBA-15, though only providing relatively low-resolution structural information.[34] Meanwhile, our recent study demonstrated the capability of SANS to unveil the spatial arrangement of immobilized deuterated green fluorescence protein (d-GFP) within hierarchically mesoporous MOF-919.[31] The findings indicate that GFP molecules are closely packed within the cavities and interact with each other through interconnected windows to form small protein "clusters".

With this in mind, we initiated this study with the aim of revealing enzyme arrangement within spatially confined cavities, particularly in mesoporous MOFs, using a hydrogenated enzyme loaded into large, highly ordered single crystals. Interestingly, upon revisiting our earliest work encapsulating cytochrome c (Cyt. c) into Tb-mesoMOF crystals, new findings suggest that the extended enzyme loading process could be adjusted by introducing enzymes under varying buffer concentrations, leading to the formation of enzyme clusters in the cavities. To overcome the limitations of traditional pathways, we employed the technique of contrast-matching small-angle neutron scattering (CM-SANS) to study the overall structures of immobilized biomolecules in MOFs. Length scales of SANS (from 1 to 200 nm) have been demonstrated to be well-fitted with the scale of the permanent porosity of MOFs and, if present, enzyme clusters confined in the interior cavities of MOFs.[35–39] The scattering contrast originates from the differences in neutron scattering length density (NSLD) among individual components in the hybrid biocomposites. The contrast matching experiment suppresses the SANS signal of the MOF matrix at certain D_2O/H_2O ratio, thereby allowing effective extraction of the incorporated enzyme signal and enabling the resolution of its overall conformation, dimensions, and shape as an individual component. It is noteworthy that the Tb-mesoMOF treated with higher concentrations of 2-amino-2-(hydroxymethyl)propane-1,3-diol (Tris) buffer exhibited significantly enhanced migration and immobilization of Cyt. c, leading to the formation of enzyme clusters arranged within the framework. This observation is further supported by SANS results at both dry and wet states, which reveal that the successful loading and clustering of Cyt. c within Tb-mesoMOF correlates with the appearance of a broad scattering hump in the low-q range. By employing contrast matching and data modelling, we were able to isolate the scattering contribution from the accommodated Cyt. c and subsequently resolve the spatial arrangement of a ~59.4 nm superstructure inside Tb-mesoMOF.

Results and Discussion

Herein, we present comprehensive scattering data under different conditions in a highly crystalline and hierarchical mesoporous MOF, Tb-mesoMOF using regular enzyme Cyt. c (Figure 1). The large nanocages of Tb-mesoMOF are seemingly the primary candidate for encapsulating bulky enzymes, and those large interior cavities are proposed to isolate the enclosed enzymes effectively, preventing them from aggregation and self-digestion. Tb-mesoMOF, also known as Tb-TATB, is a terbium-based mesoporous MOF, coordinated by 4, 4′, 4″-s-triazine-2,4,6-triyl-tribenzoic acid (H_3TATB) and Tb^{3+} to form truncated super tetrahedrons (Figure 1a) and two mesopores (Figure 1b,d).[40] The small mesopore (the blue in Figure 1b,d) is reported to be 3.9 nm in diameter, with a measured pore size of ~3.0 nm, surrounded by 12 pentagonal windows (the diameter is 1.3 nm). The large nanocage (the red in Figure 1b,d) is 4.7 nm, with a measured pore diameter of ~4.1 nm, having 12 pentagonal and 4 hexagonal windows (the diameter is 1.7 nm). These two mesopores are well-fitted with Cyt. c (2.5 × 3.2 × 3.7 nm^3, 12k Da, Figure 1c), and the neighbouring pores are fused through pentagonal windows, while hexagonal windows connect two large mesocages. The well-defined geometric properties of the chosen Tb-mesoMOF allow for ease in experimental conduction, characterization, and modelling using the technique of SANS.

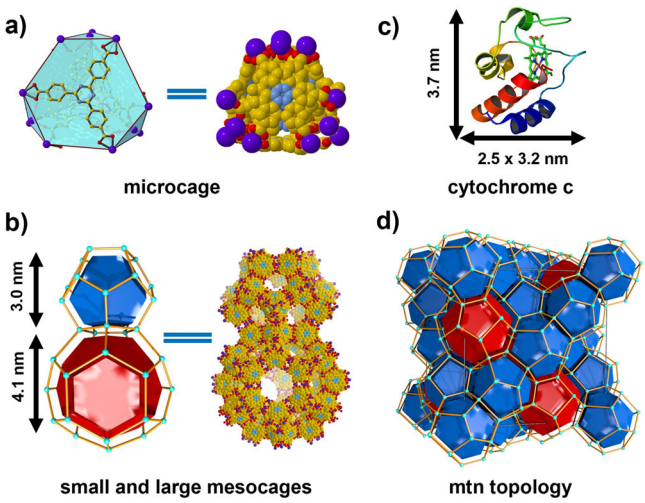

Figure 1. Structure of Tb-mesoMOF, including a) microporous truncated tetrahedron (cyan sphere in mtn topology), b) two connected mesopores (blue represents small mesopore and red represents large mesopore). c) The structural dimensions of Cyt. c, and d) mtn topology of Tb-mesoMOF. Color scheme (C: yellow, N: blue, O: red, Tb: purple).

The pore geometry of unloaded Tb-mesoMOF was first determined by SANS in the dry state (Figure 2). The SANS profiles are categorized into three regimes, associated with the pore geometry of MOF and its hierarchical structures. The low q region of 0.003–0.02 $Å^{-1}$, follows a mass fractal, as indicated by the power law exponent of −2.95. The mass fractal is formed by the network of aggregated mesopores. In the middle q range, the scattering hump in the q range of 0.02–0.06 $Å^{-1}$ presumably associated with structural irregularities or variations in density. There are three correlation peaks located in the high q range of 0.06–0.4 $Å^{-1}$, associated with three distinct pores in Tb-mesoMOF, including one micropore and two mesopores. The solid red line in Figure 2 represents the best fit of the full curve, obtained using a combined model

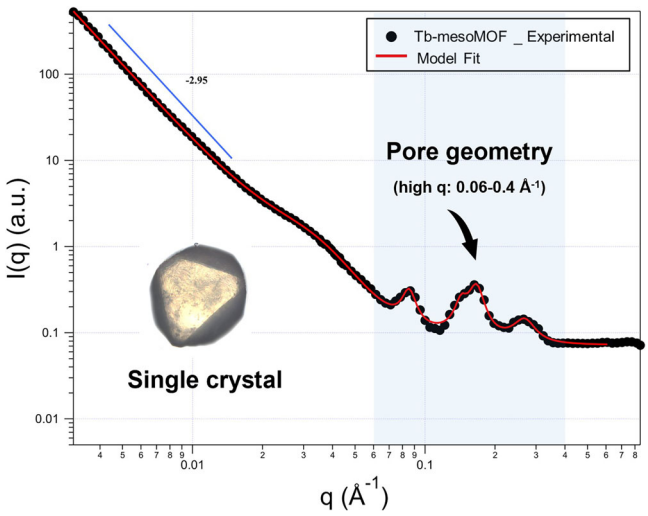

Figure 2. SANS profile of guest-free Tb-mesoMOF and the corresponding model fit. The solid red line corresponds to the best fit using the summed model, including a power law for surface scattering, a correlation length model for disordered pores, Gaussian functions for the Bragg correlation peaks, and an incoherent scattering background.

that includes a power law for surface scattering, a correlation length model for disordered pores, three Gaussian functions for the Bragg correlation peaks, and an incoherent scattering background (Table S1). To illustrate, SANS patterns of the empty Tb-mesoMOF show three distinct Bragg peaks at q = 0.0824, 0.16, and 0.263 $Å^{-1}$, reflecting well-defined long-range ordering. Under the reflection conditions of the F(–4)3 m space group, these peaks correspond to the (111), (311), and (511) reflections of the fcu-derived network. Because neutron scattering probes NSLD contrast between the metal–oxo clusters and the pore regions, these high q peaks represent the mesoscopic periodicity of the pore–node architecture. Changes in these features therefore provide a direct and sensitive indicator of structural evolution within Tb-mesoMOF during or after enzyme immobilization.

To effectively assess the spatial arrangement of Cyt. c in Tb-mesoMOF and exclude interference from Tb-mesoMOF structural components, contrast-matching experiments were carried out before SANS measurements of enzyme-loaded MOF (details in Supporting Information Section 2.2). Neutron contrast is determined by the isotopic composition of both the particle and the solvent, based on the ubiquitous existence of hydrogen in biomolecules and the dependence on the isotopic composition of scatterers and their surrounding medium. This characteristic makes CM-SANS an exceptionally powerful tool in neutron scattering, a capability that is not available in other scattering techniques, such as X-ray scattering, due to the differences in scattering densities between components. The NSLD of Tb-mesoMOF was calculated to be approximately 1.75×10^{-6} $Å^{-2}$ based on a skeletal density of 0.57 g/cm^3, which was determined from the previously reported structure file.[40] The calculated contrast matching point, where the solvent SLD matches the NSLD of Tb-mesoMOF, occurs at approximately 34% D_2O and 66% H_2O in the solvent mixture. To accurately determine the experimental contrast-matching point for Tb-mesoMOF, a series of mixtures with varying volume ratios of H_2O and D_2O (40%, 60%, 80%, and 100% D_2O) were employed to saturate the composites (Figure S6). The optimal contrastmatching ratio was identified as 60% D_2O and 40% H_2O (Figure S4 and Table S2), which is higher than the calculated value. The reported contrast-matching point for Cyt. c is approximately 41% D_2O,[41,42] thereby allowing for the extraction of the unmatched enzyme's scattering signal to be extracted at 60% D_2O. This means that, at the contrast-matching point, the scattering profile of Tb-mesoMOF is minimized and, thus the scattering intensity of the accommodated enzymes become more prominent.

The red curve in Figure 3a shows the scattering profiles of unloaded Tb-mesoMOF at the contrast-matching condition in 60% D_2O. The disappearance of high q peaks of unloaded Tb-mesoMOF in water indicates that ordered pores are accessible to water, compared with Tb-mesoMOF in the dry state (black curve). Concurrently, the low q scattering intensity dropped due to the contrast change between the framework and surrounding environment caused by the penetration of solvent into the disordered pores. Interestingly, the scattering hump position shifted to lower q, which indicates that the contrast-matching fluid adjusts the visibilities of different structural irregularities with specific length scales. In addition, the residual scattering at low q regime arises from inaccessible mesopores and density inhomogeneity, and the increased background of Tb-mesoMOF in the wet state (red curve in Figure 3a) is attributed to the incoherent scattering of H_2O. The successful loading of enzymes results in the reappearance of high q peaks, which, although weak, are still noticeable. This shift occurs due to the contrast change induced by the entry of proteins into the nanopores. Additionally, a prominent hump peak appears in the low q range, both in the dry state and within the contrast-matching solvent following enzyme loading, as shown by the green and blue curves in Figure 3a. This scattering feature reflects the presence of larger cavities formed in the material, which allow the accommodation of bulky enzyme molecules. Noteworthily, defective MOFs have been demonstrated the capability to encapsulate a wider range of biomolecule sizes, enabling the construction of multifunctional hybrid biocatalysts.[22,43,44] While it is widely acknowledged that defects typically form during the synthesis of pristine MOFs or post-synthetic modification,[45] it is less commonly recognized how buffer concentration and species, particularly under acidic or alkaline conditions, affect the enzyme loading process.

To further clarify the effects of Tris buffer on enzyme immobilization, Cyt. c facilitated Tb-mesoMOF and unloaded Tb-mesoMOF after immersion in water (25 mM NaCl), 10 mM, 20 mM, and 50 mM Tris buffer, were separately measured using CM-SANS. All samples were prepared and measured following the same procedures (see the details in the Supporting Information). Compared with the SANS profile of pristine Tb-mesoMOF, the high q of unloaded Tb-mesoMOF treated with Tris buffer shows only a weak peak at 0.4 $Å^{-1}$. This observation suggests the dramatic changes at short real-space length scales, consistent with reduced NSLD contrast due to pore filling, increased incoherent scattering

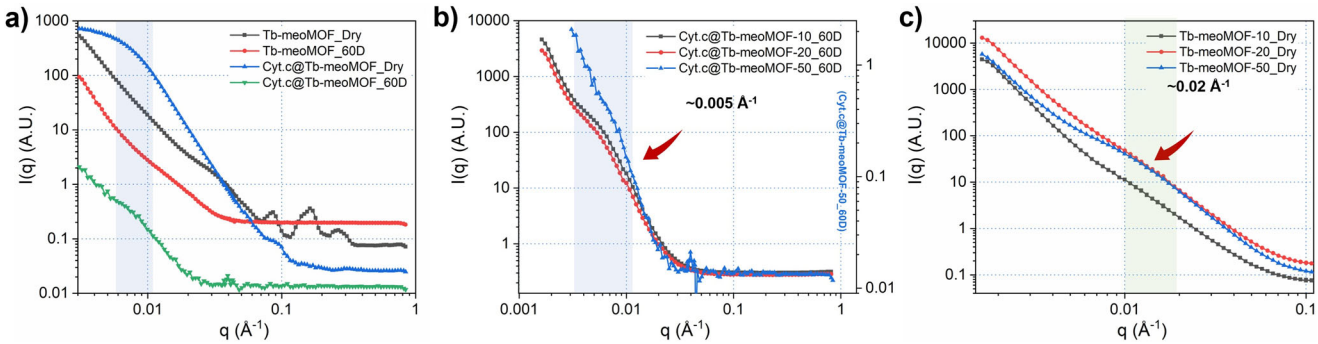

Figure 3. SANS profiles of a) unloaded Tb-mesoMOF and Cyt. c loaded Tb- mesoMOF (prepared in 50 mM Tris buffer) at dry and wet states (60% D_2O, contrast matching point), and b) Cyt. c loaded Tb- mesoMOF prepared in 10 mM, 20 mM, and 50 mM Tris buffer after the subtraction of MOF scattering at contrast matching point. A secondary y-axis is included on the right to display the Cyt c@Tb-mesoMOF-50_60D scattering profile, enabling clearer comparison with the other two wet samples. c) Scattering profiles of Tb-mesoMOF after treatment with 10, 20, and 50 mM Tris buffer in the dry state.

from hydrogen-containing buffer species, and/or local structural disorder (Figures S7–S10). However, the emergence of the hump at ~0.02 $Å^{-1}$ in Tb-mesoMOF-50 reveals the development of new large cavities (Figure 3c), with a characteristic dimension of ~31.4 nm, derived from the radius of gyration (Rg ≈ 8.7 nm) obtained using Equation 2 (Section 3 in Supporting Information). The loading of Cyt. c@Tb-mesoMOF in 10 mM, 20 mM, and 50 mM Tris buffer, resulted in a broad hump peak at 0.004–0.01 $Å^{-1}$ in the low q region (blue shading in Figure 3a,b) under both dry and wet states. This feature arises from the accommodated enzymes and reflects the formation of seemingly closely packed "clusters" within the cavity. However, this hump peak was not observed in buffer-treated empty MOFs within the same range in Figure 3c. To better depict the cluster size observed in the SANS data, the enzyme scattering was extracted from loaded samples by subtracting the background signal of unloaded Tb-mesoMOF from that of the corresponding Cyt. c@Tb-mesoMOF under the contrast matching condition (Figure 3b). The size and shape of free Cyt. c was first measured at 2 mg/mL in H_2O (75 mM and 150 mM NaCl) using prolate ellipsoid form factor and gave a volume of free Cyt. c of $1.2 \times 1.2 \times 1.0\ nm^3$ (Figure S11). Interestingly, the correlation length of this feature in Cyt. c@Tb-mesoMOF-50 was fitted to ~59.4 nm, derived from the calculated Rg of 23.0 nm (Figure S3), an averaged size distribution of enzyme cluster within the MOF framework, which is much larger than the Rg (1.2 nm) of a single Cyt. c molecule.[42] Additional intensity observed for 50 mM Cyt. c@Tb-mesoMOF over 10- and 20-mM samples can be explained by the higher loading amount of Cyt. c in more cavities (Figure S12).

We subsequently discovered that Tb-mesoMOF treated with different concentrations of Tris buffer (10-50 mM), affects the loading performance of Cyt. c and structural changes of Tb-mesoMOF. The Cyt. c loading rates in Tb-mesoMOF were systematically monitored by UV–vis spectroscopy, with samples prepared in a series of Tris buffer concentrations—0 mM (where 25 mM NaCl was added for protein stability), 10 mM, 20 mM, and 50 mM (Figure 4a). The uptakes of Cyt. c was determined, giving values of 1.8 (±6.3), 11.2 (±1.0), 57.2 (±8.2), and 138.9 (±29.1) mg/g, respectively, calculated from the concentration changes before and after 90-hour loading period (Figure 4b and Figures S13 and 14). It is important to note that no significant concentration change was observed when Tb-mesoMOF was saturated in 25 mM NaCl with 5 mg/mL Cyt. c. However, the sample treated with 50 mM Tris buffer showed the fastest and highest loading profile, approximately twice as fast as the 20 mM group and about ten times faster than the 10 mM group over the same period. This is consistent with the colour of crystalline Tb-mesoMOF from microscope images (the insets in Figure 4b and Figure S15). The crystal colour changed to red and dark red for loading Cyt. c in 10 mM, 20 mM, and 50 mM Tris but exhibited very light-brown crystals for Tb-mesoMOF treated with Cyt. c in 25 mM NaCl. Fourier Transform Infrared Spectroscopy (FTIR) analysis of all enzyme-loaded samples reveals the appearance of characteristic amide I peaks of Cyt. c at 1645 cm^{-1}, with intensified peaks observed when treated at the higher concentration of Tris buffer, corresponding to increased enzyme loading (Figure S16). Additionally, the redshift of the carboxylate ($-COO^-$) stretching vibrations from 1599 cm^{-1} to 1595 cm^{-1} indicates subtle changes in the local metal centre environment of MOF framework, likely arising from weak enzyme–framework interactions. The thermogravimetric analysis (TGA) of Cyt. c-loaded Tb-mesoMOF shows weight loss at 300 °C, corresponding to the degradation of the immobilized enzyme (Figure S17). The largest mass loss, approximately 11.3 wt%, is observed for the Cyt. c-loaded Tb-mesoMOF prepared in 50 mM Tris buffer, which aligns closely with the loading amount of 12.2 wt%.

In Tb-mesoMOF, the Tb4 cluster was connected to a trigonal-planar geometry, serving as the metal nodes in Tb-mesoMOF. The coordination pattern of each pair of TATB ligands on each face of the super-tetrahedron with nine Tb^{3+} ions is very delicate; thus, it possibly causes easy defection under alkaline buffer conditions. To investigate the generality of buffer effects on the structural integrity of Tb-mesoMOF, we treated Tb-mesoMOF with various buffers (MOPS, HEPES, PIPES, and Bis-Tris) at different pH levels (6.5 and 7.5) within their effective pH ranges. Bis-Tris was selected due to its effective function within a pH

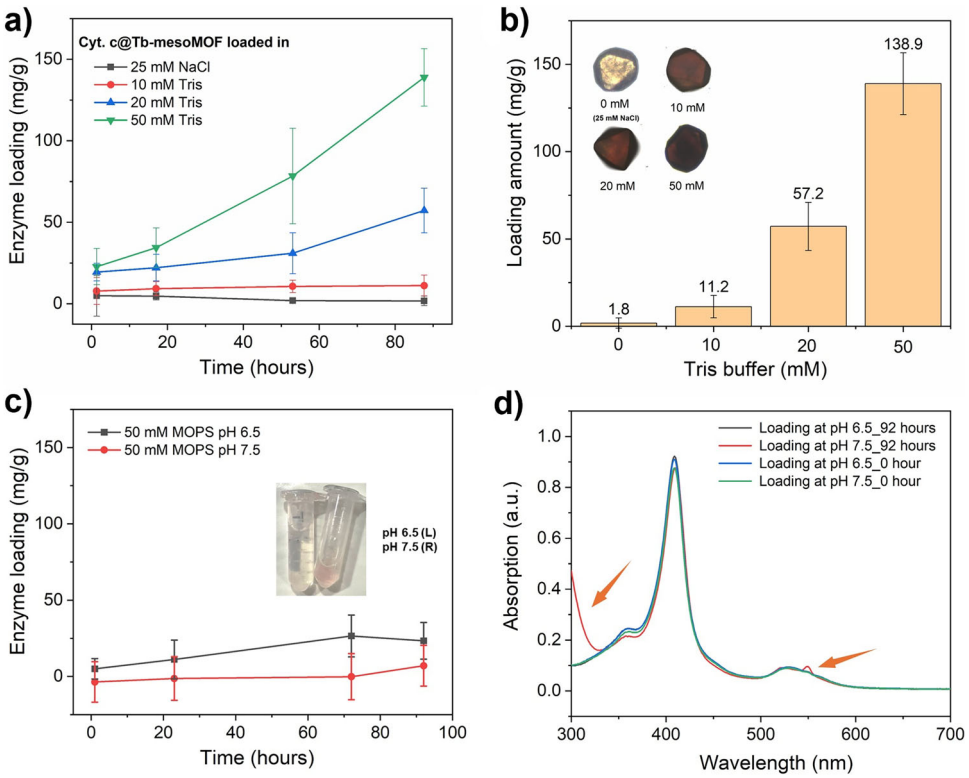

Figure 4. Enzyme loading profiles of Tb-mesoMOF in the presence of 20 mM NaCl and varying concentrations of Tris buffer (10, 20, and 50 mM), illustrating a) the loading rate of Cyt. c over time, and b) the total loading amount achieved after 90 h. c) Enzyme loading profiles of Tb-mesoMOF in the presence of 50 mM MOPS at pH 6.5 and 7.5; and d) the corresponding UV–vis spectra at 0 and 92 h. The orange arrow indicates partial structural degradation. Error bars represent the standard deviations in triplicate of Cyt. c loading measurements. The data highlight the influence of buffer concentration and pH on both the kinetics and overall capacity of enzyme loading.

range of 5.8–7.2 (Tris: 7–10), and structural similarity. Bis-Tris has two additional hydroxyethyl ($-CH_2CH_2OH$) groups alongside three hydroxymethyl ($-CH_2OH$) groups, whereas Tris contains only an amine group and three hydroxymethyl groups. The combined results of PXRD and gas adsorption indicate that pH plays a crucial role in their structural stability, with alkaline conditions having a more detrimental impact on the integrity of Tb-mesoMOF. Specifically, all samples exhibit a broad hump peak at a lower 2θ in their PXRD patterns, suggesting structural modifications (Figure S18). Among them, MOPS (pH 6.5) induces the least structural change, whereas Bis-Tris treatment results in a complete loss of crystallinity, which aligns with its negligible N_2 adsorption (Figure S19). A decrease in N_2 uptake is observed across all buffer-treated samples (Figures S20–S23), though the effects are less pronounced at pH 6.5, except in the case of Bis-Tris. Additionally, a notable increase in total mass (Figure S24) suggests that buffer molecules were adsorbed into MOFs.

Since PXRD analysis revealed that MOPS buffer at pH 6.5 exerted the least influence on the structural integrity of Tb-mesoMOF, enzyme loading experiments were subsequently carried out using 50 mM MOPS at pH 6.5 and 7.5 to evaluate loading performance. In both cases, Cyt. c uptake was very low (Figure 4c). Crystals obtained at pH 6.5 remained colourless, whereas those at pH 7.5 developed a faint red coloration (inset in Figure 4c), aligned well with the larger PSD at pH 7.5 (Figure S22). After 92 h, the UV–vis spectrum of the pH 7.5 sample displayed two additional peaks at ~550 nm and ~350 nm (Figure 4d), which may be attributed to the release of MOF fragment, and could lead to an underestimation of the loading amount of Cyt. c. These results indicate that buffer species and pH play very critical roles in Cyt. c loading into Tb-mesoMOF, with alkaline conditions more likely to compromise structural integrity.

To investigate the changes of pore size and volume, the N_2 isotherms at 77 K and pore size distributions (PSD) based on their N_2 isotherms were systematically investigated, regarding the unloaded Tb-mesoMOF and Cyt. c @Tb-mesoMOF after treatment with varying concentrations of Tris buffer, as shown in Figure 5. The N_2 isotherms at 77 K revealed that the Brunauer – Emmett – Teller (BET) area of Cyt. c loaded Tb-mesoMOF prepared in 10 mM, 20 mM, and 50 mM Tris dramatically decreased, were measured as 1100, 480, and 275 m^2/g, respectively (Figure 5a). Meanwhile, the surface areas of Tb-mesoMOF after treatment with Tris buffer at concentrations of 10 mM, 20 mM, and 50 mM, also dropped significantly from 1550 to 870, 620, and 270 m^2/g, respectively (Figure 5d). Notably, Tb-mesoMOF exhibits a slightly lower surface area after being treated with 25 mM NaCl, demonstrating its moderate aqueous stability. Compared to pristine Tb-mesoMOF, the DFT-based PSD analysis of Tris buffer–treated samples reveals a significant

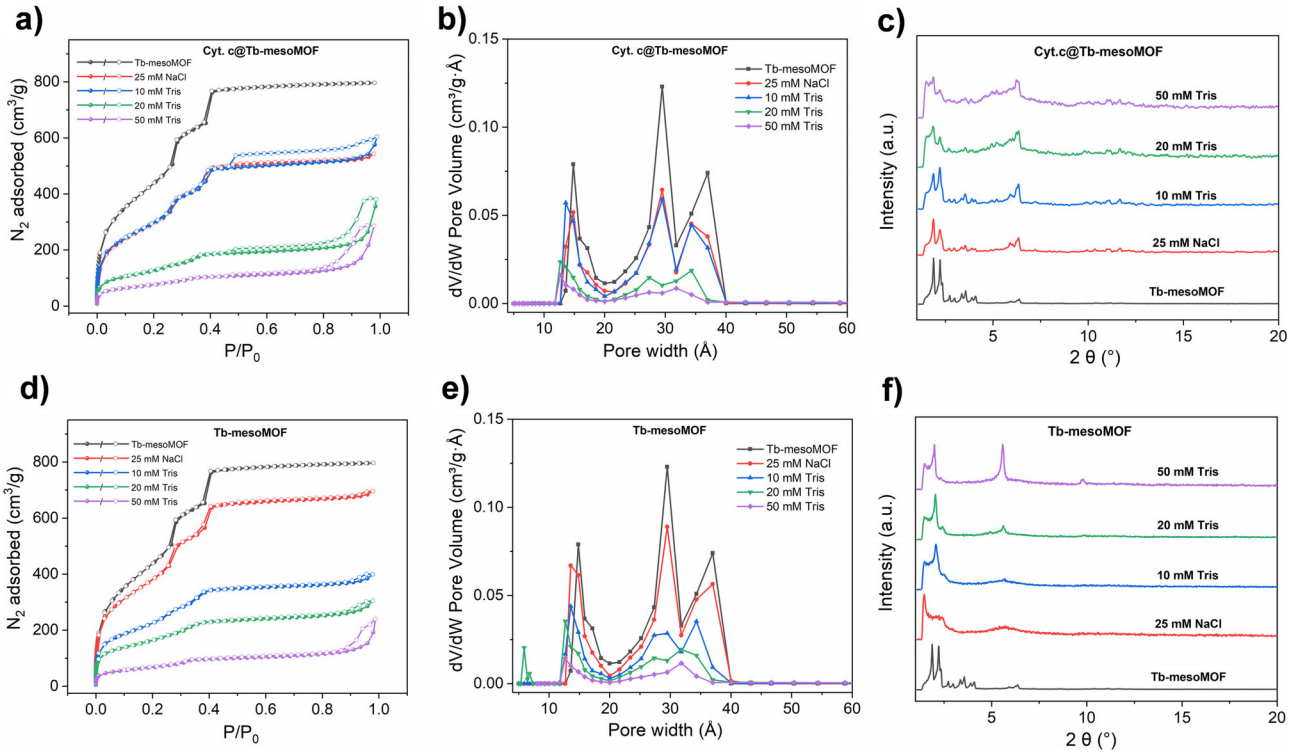

Figure 5. Profiles of Cyt. C loaded Tb-mesoMOF and unloaded Tb-mesoMOF treated with 20 mM NaCl and varying concentrations of Tris buffer (10, 20, and 50 mM) at pH 7.6, including (a, d) N_2 isotherms at 77 K, (b, e) DFT-calculated pore size distribution based on their N_2 isotherms, and (c, f) PXRD.

reduction in the pore volumes of two mesopores (Figure 5b,e), accompanied by an increase in pore volume at larger cavities (Figures S25–S27) in a concentration-dependent manner. To illustrate, the Barrett–Joyner–Halenda (BJH) PSD method was employed, as it is most reliable for analyzing mesopores in the 2–50 nm range. While pristine Tb-mesoMOF, Tb-mesoMOF-0, and Cyt c@Tb-mesoMOF-0 show negligible pore-volume contributions between 5 and 50 nm, both Tb-mesoMOF and Cyt c@Tb-mesoMOF treated with 50 mM Tris buffer exhibit a pronounced increase in pore volume within this range. This observation is fully consistent with the SANS results, which indicate the formation of newly generated large cavities within the framework under higher Tris concentrations. Meanwhile, the PXRD patterns of all buffer-treated Tb-mesoMOF show the emergence of a new peak at a lower 2θ value of 1.48°, positioned to the left of the first peak in pristine Tb-mesoMOF. This shift also suggests an expansion of the unit cell, likely due to framework modifications such as the formation of larger cavities (Figure 5f).

However, this effect is less pronounced in the presence of the enzyme under the same buffer conditions, suggesting that the MOF structure likely remains more intact due to the stabilizing influence of the hosted enzyme within the cavities (Figure 5c). This also contributes to the observed pore volume loss in Cyt. c-loaded Tb-mesoMOF besides decomposition (Figure S27). These findings highlight that the acidic or alkaline nature of the buffer and its functional groups can significantly influence the structural integrity of MOF matrix, potentially providing excessive pathways and space for enzyme migration and clustering.

Conclusions

In summary, this work used SANS combined with complementary techniques to investigate the spatial arrangement of immobilized enzyme within a highly crystalline MOF. It emphasizes that the immobilization efficiency of Cyt. c in Tb-mesoMOF was significantly enhanced by buffer solutions, enabling the multiple Cyt. c molecules to be encapsulated within a single cavity and eventually form enzyme "clusters" with high packing density and close contact. The unique feature of contrast matching SANS allows effective extraction of structure information from the confined enzymes, while minimizing the interference from scattering by the host MOF. This work exploits a novel pathway to investigate the spatial arrangement of immobilized enzymes and establishes a methodology in combination of the advanced technique of SANS and complementary characterizations. Clarifying enzyme behavior and arrangement in confined environments will assist our understanding of enzymatic performance under various conditions. More importantly, it provides a new perspective and a vital attempt to study the enzyme behavior in bulky crystal MOFs in a more straightforward way.

Acknowledgements

The authors acknowledge the financial support from the US National Science Foundation (DMR-1352065) and the Robert A. Welch Foundation (B-0027). Partial support from U.S. Army Contracting Command (W52P1J-21–9–3023) is

also acknowledged (OKF). Neutron scattering experiments on Bio-SANS were supported by the Center for Structural Molecular Biology funded by DOE Biological and Environmental Research (ERKP291). A portion of this research used resources at the High Flux Isotope Reactor, a DOE Office of Science User Facility operated by the Oak Ridge National Laboratory (IPTS-27697, IPTS-18982 and IPTS-20263).

Conflict of Interests

O.K.F. has a financial interest in NuMat Technologies, a startup company that is seeking to commercialize MOFs.

Data Availability Statement

The data that support the findings of this study are available from the corresponding author upon reasonable request.

Keywords: Enzyme cluster · Enzyme immobilization · MOFs · SANS

[1] J. Liang, K. Liang, *Adv. Funct. Mater.* **2020**, *30*, 2001648, https://doi.org/10.1002/adfm.202001648.
[2] S. Huang, X. Kou, J. Shen, G. Chen, G. Ouyang, *Angew. Chem. Int. Ed.* **2020**, *59*, 8786–8798, https://doi.org/10.1002/anie.201916474.
[3] R. A. Sheldon, S. van Pelt, *Chem. Soc. Rev.* **2013**, *42*, 6223–6235, https://doi.org/10.1039/C3CS60075K.
[4] A. S. Bommarius, M. F. Paye, *Chem. Soc. Rev.* **2013**, *42*, 6534, https://doi.org/10.1039/c3cs60137d.
[5] J. M. Choi, S. S. Han, H. S. Kim, *Biotechnol. Adv.* **2015**, *33*, 1443–1454, https://doi.org/10.1016/j.biotechadv.2015.02.014.
[6] S. Wu, R. Snajdrova, J. C. Moore, K. Baldenius, U. T. Bornscheuer, *Angew. Chem. Int. Ed.* **2021**, *60*, 88–119, https://doi.org/10.1002/anie.202006648.
[7] S. Huang, G. Chen, G. Ouyang, *Chem. Soc. Rev.* **2022**, *51*, 6824–6863, https://doi.org/10.1039/D1CS01011E.
[8] W. Liang, P. Wied, F. Carraro, C. J. Sumby, B. Nidetzky, C. K. Tsung, P. Falcaro, C. J. Doonan, *Chem. Rev.* **2021**, *121*, 1077–1129, https://doi.org/10.1021/acs.chemrev.0c01029.
[9] X. Wang, P. C. Lan, S. Ma, *ACS Cent. Sci.* **2020**, *6*, 1497–1506, https://doi.org/10.1021/acscentsci.0c00687.
[10] H. An, M. Li, J. Gao, Z. Zhang, S. Ma, Y. Chen, *Coord. Chem. Rev.* **2019**, *384*, 90–106, https://doi.org/10.1016/j.ccr.2019.01.001.
[11] M. B. Majewski, A. J. Howarth, P. Li, M. R. Wasielewski, J. T. Hupp, O. K. Farha, *CrystEngComm* **2017**, *19*, 4082–4091, https://doi.org/10.1039/C7CE00022G.
[12] X. Lian, Y. Fang, E. Joseph, Q. Wang, J. Li, S. Banerjee, C. Lollar, X. Wang, H. C. Zhou, *Chem. Soc. Rev.* **2017**, *46*, 3386–3401, https://doi.org/10.1039/C7CS00058H.
[13] W. Yang, W. Liang, L. A. O'Dell, H. D. Toop, N. Maddigan, X. Zhang, A. Kochubei, C. J. Doonan, Y. Jiang, J. Huang, *JACS Au* **2021**, *1*, 2172–2181, https://doi.org/10.1021/jacsau.1c00226.
[14] Y. M. Li, J. Yuan, H. Ren, C. Y. Ji, Y. Tao, Y. Wu, L. Y. Chou, Y. B. Zhang, L. Cheng, *J. Am. Chem. Soc.* **2021**, *143*, 15378–15390, https://doi.org/10.1021/jacs.1c07107.
[15] G. Chen, X. Kou, S. Huang, L. Tong, Y. Shen, W. Zhu, F. Zhu, G. Ouyang, *Angew. Chem. Int. Ed.* **2020**, *59*, 2867–2874, https://doi.org/10.1002/anie.201913231.
[16] W. Liang, H. Xu, F. Carraro, N. K. Maddigan, Q. Li, S. G. Bell, D. M. Huang, A. Tarzia, M. B. Solomon, H. Amenitsch, L. Vaccari, C. J. Sumby, P. Falcaro, C. J. Doonan, *J. Am. Chem. Soc.* **2019**, *141*, 2348–2355, https://doi.org/10.1021/jacs.8b10302.
[17] Y. Chen, V. Lykourinou, C. Vetromile, T. Hoang, L. J. Ming, R. W. Larsen, S. Ma, *J. Am. Chem. Soc.* **2012**, *134*, 13188–13191, https://doi.org/10.1021/ja305144x.
[18] J. Navarro-Sanchez, N. Almora-Barrios, B. Lerma-Berlanga, J. J. Ruiz-Pernia, V. A. Lorenz-Fonfria, I. Tunon, C. Marti-Gastaldo, *Chem. Sci.* **2019**, *10*, 4082–4088, https://doi.org/10.1039/C9SC00082H.
[19] Y. Pan, X. Wang, H. Li, J. Ren, Y. Zhang, D. Jordahl, I. Schuster, J. Farmakes, H. Hong, Z. Yang, S. Ma, *Cell Rep. Phys. Sci.* **2021**, *2*, 100576, https://doi.org/10.1016/j.xcrp.2021.100576.
[20] Y. Feng, R. Shi, M. Yang, Y. Zheng, Z. Zhang, Y. Chen, *Angew. Chem. Int. Ed.* **2023**, *62*, e202302436, https://doi.org/10.1002/anie.202302436.
[21] Z. Li, T. M. Rayder, L. Luo, J. A. Byers, C. K. Tsung, *J. Am. Chem. Soc.* **2018**, *140*, 8082–8085, https://doi.org/10.1021/jacs.8b04047.
[22] F. Sha, H. Xie, K. O. Kirlikovali, W. Gong, Y. Chen, O. K. Farha, *ACS Mater. Lett.* **2024**, *6*, 1396–1403, https://doi.org/10.1021/acsmaterialslett.4c00199.
[23] M. Qiao, Y. Li, Y. Li, M. Chang, X. Zhang, S. Yuan, *Angew. Chem. Int. Ed.* **2024**, *63*, e202409951, https://doi.org/10.1002/anie.202409951.
[24] P. D. Patil, N. Gargate, M. S. Tiwari, S. S. Nadar, *Coord. Chem. Rev.* **2025**, *531*, 216519, https://doi.org/10.1016/j.ccr.2025.216519.
[25] J. He, N. Li, Z. G. Li, M. Zhong, Z. X. Fu, M. Liu, J. C. Yin, Z. Shen, W. Li, J. Zhang, Z. Chang, X. H. Bu, *Adv. Funct. Mater.* **2021**, *31*, 2103597, https://doi.org/10.1002/adfm.202103597.
[26] G. Cai, P. Yan, L. Zhang, H. C. Zhou, H. L. Jiang, *Chem. Rev.* **2021**, *121*, 12278–12326, https://doi.org/10.1021/acs.chemrev.1c00243.
[27] Z. Wang, S. Henke, M. Paulus, A. Welle, Z. Fan, K. Rodewald, B. Rieger, R. A. Fischer, *ACS Appl. Mater. Interfaces* **2020**, *12*, 2655–2661, https://doi.org/10.1021/acsami.9b18672.
[28] L. Yuan, M. Tian, J. Lan, X. Cao, X. Wang, Z. Chai, J. K. Gibson, W. Shi, *Chem. Commun.* **2018**, *54*, 370–373, https://doi.org/10.1039/C7CC07527H.
[29] G. C. Shearer, S. Chavan, S. Bordiga, S. Svelle, U. Olsbye, K. P. Lillerud, *Chem. Mater.* **2016**, *28*, 3749–3761, https://doi.org/10.1021/acs.chemmater.6b00602.
[30] Y. Liu, S. Cui, W. Ma, Y. Wu, R. Xin, Y. Bai, Z. Chen, J. Xu, J. Ge, *J. Am. Chem. Soc.* **2024**, *146*, 12565–12576, https://doi.org/10.1021/jacs.4c01483.
[31] X. Wang, L. He, J. Sumner, S. Qian, Q. Zhang, H. O'Neill, Y. Mao, C. Chen, A. M. Al-Enizi, A. Nafady, S. Ma, *Nat. Commun.* **2023**, *14*, 973, https://doi.org/10.1038/s41467-023-36533-w.
[32] S. Perticaroli, G. Ehlers, C. B. Stanley, E. Mamontov, H. O'Neill, Q. Zhang, X. Cheng, D. A. Myles, J. Katsaras, J. D. Nickels, *J. Am. Chem. Soc.* **2017**, *139*, 1098–1105, https://doi.org/10.1021/jacs.6b08845.
[33] R. D. Santos Morais, O. Delalande, J. Perez, L. Mouret, A. Bondon, A. Martel, M. S. Appavou, E. Le Rumeur, J. F. Hubert, S. Combet, *Langmuir* **2017**, *33*, 6572–6580, https://doi.org/10.1021/acs.langmuir.7b01369.
[34] J. Siefker, R. Biehl, M. Kruteva, A. Feoktystov, M. O. Coppens, *J. Am. Chem. Soc.* **2018**, *140*, 12720–12723, https://doi.org/10.1021/jacs.8b08454.
[35] L. He, A. Piper, F. Meilleur, D. A. Myles, R. Hernandez, D. T. Brown, W. T. Heller, *J. Virol.* **2010**, *84*, 5270–5276, https://doi.org/10.1128/JVI.00044-10.
[36] T. R. Sosnick, S. A. Woodson, *Biopolymers* **2011**, *95*, 503–504, https://doi.org/10.1002/bip.21643.
[37] B. J. Heuser, J.-L. Lin, C. Do, L. He, *J. Appl. Crystallogr.* **2018**, *51*, 768–780, https://doi.org/10.1107/S160057671800479X.

[38] Y. Mao, K. Liu, C. Zhan, L. Geng, B. Chu, B. S. Hsiao, *J. Phys. Chem. B* **2017**, *121*, 1340–1351, https://doi.org/10.1021/acs.jpcb.6b11425.
[39] R. P. Rambo, J. A. Tainer, *Nature* **2013**, *496*, 477–481, https://doi.org/10.1038/nature12070.
[40] Y. K. Park, S. B. Choi, H. Kim, K. Kim, B. H. Won, K. Choi, J. S. Choi, W. S. Ahn, N. Won, S. Kim, D. H. Jung, S. H. Choi, G. H. Kim, S. S. Cha, Y. H. Jhon, J. K. Yang, J. Kim, *Angew. Chem. Int. Ed.* **2007**, *46*, 8230–8233, https://doi.org/10.1002/anie.200702324.
[41] D. A. Jacques, J. Trewhella, *Protein Sci.* **2010**, *19*, 642–657, https://doi.org/10.1002/pro.351.
[42] S. L. Freeman, A. Martel, J. M. Devos, J. Basran, E. L. Raven, G. C. K. Roberts, *J. Biol. Chem.* **2018**, *293*, 5210–5219, https://doi.org/10.1074/jbc.RA118.001941.
[43] X. Liu, W. Qi, Y. Wang, D. Lin, X. Yang, R. Su, Z. He, *ACS Appl. Mater. Interfaces* **2018**, *10*, 33407–33415, https://doi.org/10.1021/acsami.8b09388.
[44] L. Li, T. Wang, Z. Xu, W. Zhou, X. F. Yu, *Nanoscale* **2022**, *14*, 3929–3934, https://doi.org/10.1039/D1NR07826G.
[45] L. Feng, S. Yuan, L. L. Zhang, K. Tan, J. L. Li, A. Kirchon, L. M. Liu, P. Zhang, Y. Han, Y. J. Chabal, H. C. Zhou, *J. Am. Chem. Soc.* **2018**, *140*, 2363–2372, https://doi.org/10.1021/jacs.7b12916.

Manuscript received: October 20, 2025
Revised manuscript received: November 19, 2025
Manuscript accepted: November 24, 2025
Version of record online: ■■, ■■